

Low-Temperature Thermoelectric Performance and Optoelectronic Properties of Monolayer of WX_2N_4 ($X = Si, Ge$).

Chayan Das^a, Dibyajyoti Saikia^a, Atanu Betal^a, Satyajit Sahu*

^a Department of Physics, Indian Institute of Technology Jodhpur, Jodhpur 342037, India

Abstract

Two-dimensional (2D) materials proved their suitability for thermoelectric applications due to specific quantum confinement and distinct density of states (DOS). New two-dimensional layered materials WX_2N_4 ($X = Si, Ge$) are suitable for thermoelectric applications with a quite satisfactory value of ZT . Here we investigated the thermoelectric properties of the 2D monolayer of WX_2N_4 ($X = Si, Ge$) by using Density Functional Theory (DFT) combined with Boltzmann Transport Equation (BTE). We obtained an outstanding thermoelectric figure of merit (ZT) of 0.91 at 400K for p-type WGe_2N_4 , whereas it showed a ZT value of 0.56 for n-type at the same temperature. On the other hand, the WSi_2N_4 showed significantly low ZT at room temperature. However, the ZT value increases significantly at higher temperatures. We examined the electrical property and discovered that the indirect bandgaps (BG) of WSi_2N_4 and WGe_2N_4 are 2.00 eV and 1.15 eV, respectively. In the deep ultraviolet (UV) and UV areas, they displayed very strong absorption. Due to their strong absorption, these materials may also be used in thermoelectric applications and (solar-blind) UV optoelectronic devices.

1. Introduction

The search for materials to fabricate highly efficient thermoelectric generators is trending research. Metal chalcogenides, alloys¹⁻⁶, and their oxides⁷⁻⁹ made up the majority of the thermoelectric material regime. Bi_2Te_3 ¹⁰, $SnSe$ ¹¹, and $PbTe$ ¹² possess very high ZT value among them. After the discovery of graphene 2D transition metal dichalcogenides (TMDC) also attracted our attention because of their extraordinary optical¹³, electronic¹⁴, and thermal¹⁴ properties. Recently new 2D monolayer of $MoSi_2N_4$ was deposited using the CVD method in centimeter scale¹⁵. So, we are motivated to explore the properties of these monolayers. These materials possess very high dynamical stability and very high mechanical properties¹⁶.

Electricity can be generated from waste heat using these materials. Renewable energy sources are crucial in the current period since non-renewable energy sources are rapidly running out. In this work, we investigated the 2D monolayer of WSi_2N_4 and WGe_2N_4 using Boltzmann transport theory in association with DFT, and we found very high Seebeck coefficients (S). The seebeck coefficient of a material is the measure of the magnitude of induced voltage generated when a temperature difference is introduced between the two ends of the material. For efficient thermoelectric material, both the electrical conductivity (σ) and S should be high, and the thermal conductivity ($k = k_{el} + k_{ph}$) should be low. The thermal conductivity k has two components, k_{el} , and k_{ph} , which represents the contribution coming from electrons and phonons respectively. Generally, these 2D materials possess high mobility, excellent stability and good optoelectronic and piezoelectric properties¹⁶. These materials can be represented by N-X-N-M-N-X-N. Metal atom (M) was sandwiched in between two nitrogen (N) atoms, and the whole system was sandwiched between buckled honeycomb XN layer where X = Si or Ge. Here M is the transition metal atom (Mo, W, Ti, Cr, etc.). They can be synthesized using chemical vapor deposition (CVD). Yi-Lun Hong et al. synthesized MoSi_2N_4 using CVD¹⁵. Bohayra Mortazavi predicted mobility of 490 and 2190 $\text{cm}^2\text{V}^{-1}\text{s}^{-1}$ for p and n-type of monolayer MoSi_2N_4 ¹⁶. Till now, many good researches have been carried out by researchers on 2D TMDC materials. Huang et al. and his group reported a very low ZT value < 0.2 , along with a high thermal conductivity of about 60 W/m K, with MoSe_2 monolayer. SD Guo and co-workers reported a ZT value greater than 0.9 at 600K with ZrS_2 monolayer along with a thermal conductance of 47.8 W/K, respectively. Monolayer MoS_2 and WS_2 were also reported with very high k_{ph} of 23.15 W/mK and 72 W/m.K¹⁷. But monolayer HfS_2 was reported with very low k_{ph} of 2.83 W/mK along with a very good ZT i.e. $ZT_{\text{HfS}_2} = 0.90$ ¹⁸. Many researches are still going on to improve the ZT factor of materials. In this work, we systematically investigated with great detail the electronic, optical, and thermoelectric properties of monolayers of WSi_2N_4 and WGe_2N_4 using DFT and BTE. In the WGe_2N_4 monolayer, we found an outstanding ZT product of 0.91 for p-type (0.56 for n-type) at a very low temperature of 400K. Similarly, the WSi_2N_4 monolayer showed a poor ZT of 0.26 for p-type (0.05 for n-type). Thus, we need a theoretical investigation of thermoelectric and optical properties to understand the physical and chemical properties that cause the huge difference in their efficiency towards thermoelectric application necessitates. WSi_2N_4 showed high absorption in the deep UV region (285 nm), whereas

WGe₂N₄ showed strong absorption in the UV region (306 nm), making the materials usable in UV optoelectronic applications beyond the visible spectrum.

2. Methodology

We accomplished the first principle calculations using DFT with projector augmented wave (PAW) potentials^{19,20} and Perdew-Burke-Ernzerhof (PBE) as generalized gradient approximation (GGA)²¹ in Quantum Espresso (QE) package. To avoid the interaction of two layers, we kept a vacuum of 30 Å between two layers along the z-direction. The geometry optimization was performed using a 15×15×1 k-mesh grid. A wave function energy cutoff of 50 Ry and self-consistency of 10⁻⁹ Ry were kept in all the calculations. The atoms were relaxed until the force convergent threshold of 3.8×10⁻⁴ Ry was achieved. We used the Phonopy package combined with QE to evaluate the phonon dispersion band structure using 2×2×1 supercell with 9×9×1 k-mesh in the QE package. The optical properties were evaluated using the SIESTA package, which is implemented with Time-Dependent Density Functional Perturbation Theory (TD-DFPT)²². A 48×48×1 k-mesh was used for the calculation of the optical properties. We obtained the imaginary (ϵ_i) and real (ϵ_r) parts of dielectric functions using Momentum space formulation along with Kramers-Kronig transformation²³. After, that we obtained the absorption coefficient (α), refractive index (η), and extinction coefficient (K) using the following equations.

$$\eta = \left[\frac{\{(\epsilon_r^2 + \epsilon_i^2)^{1/2} + \epsilon_r\}}{2} \right]^{1/2} \quad (1)$$

$$K = \left[\frac{\{(\epsilon_r^2 + \epsilon_i^2)^{1/2} - \epsilon_r\}}{2} \right]^{1/2} \quad (2)$$

$$\alpha = \frac{2K\omega}{c} \quad (3)$$

Here, ϵ_r , ϵ_i , ω , and C are real and imaginary parts of the dielectric function, frequency, and speed of light, respectively. Thermoelectric parameters were obtained using constant scattering time approximation from BoltzTraP code²⁴ using the Boltzmann transport equation.

$$\sigma_{l,m} = \frac{1}{\Omega} f \sigma_{l,m}(\epsilon) \left[-\frac{\Delta f_{\mu}(T,\epsilon)}{\Delta \epsilon} \right] d\epsilon \quad (4)$$

$$k_{l,m}(T, \mu) = \frac{1}{e^2 T \Omega} f \sigma_{l,m}(\epsilon) (\epsilon - \mu)^2 \left[-\frac{\Delta f_{\mu}(T,\epsilon)}{\Delta \epsilon} \right] d\epsilon \quad (5)$$

$$S_{l,m}(T, \mu) = \frac{(\sigma^{-1})_{n,l}}{eT\Omega} \int \sigma_{n,m}(\varepsilon)(\varepsilon - \mu) \left[-\frac{\Delta f_{\mu}(T, \varepsilon)}{\Delta \varepsilon} \right] d\varepsilon \quad (6)$$

Using these equations, we obtained the transport properties. Here, $\sigma_{l,m}$, $k_{l,m}$, $S_{l,m}$, are the electrical conductivity, thermal conductivity, and Seebeck coefficient, respectively. Whereas e, μ, Ω, T are the electron charge, chemical potential, unit cell volume, and temperature, respectively. The phono3py package combined with QE was used to evaluate the k_{ph} . In phono3py, a $2 \times 2 \times 1$ supercell with $9 \times 9 \times 1$ k-mesh was generated, and self-consistent calculations were performed using a default displacement of 0.06 Å.

3. Result and Discussions

3.1. Structural Properties and Stability

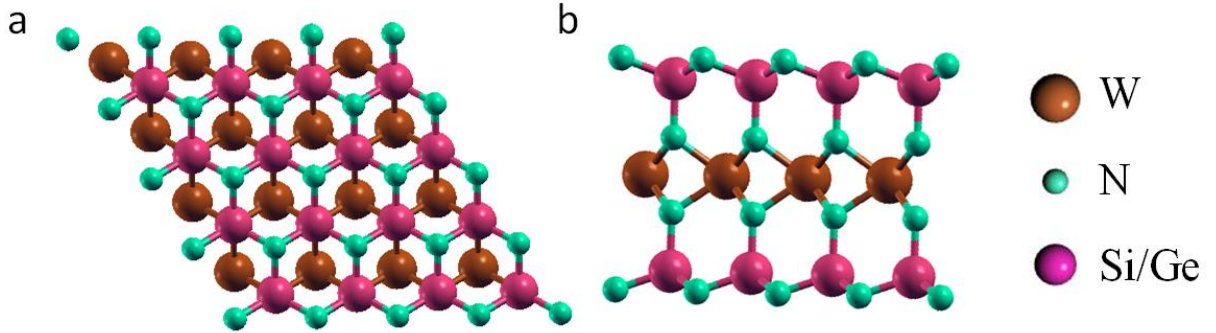


Figure.1: (a) Top and (b) side view of WX_2N_4 monolayer with honeycomb structure of $4 \times 4 \times 1$ supercell.

WX_2N_4 ($X = \text{Si}, \text{Ge}$) monolayer can be viewed as a WN_2 monolayer sandwiched between two honeycomb (SiN/GeN) layers. The three layers are stacked on each other. W atom is located at the center of a trigonal prism building block with six Si atoms, and the WN_2 layer is bonded to (SiN/GeN) layers via vertically aligned Si–N bonds (figure 1(a)). WX_2N_4 possesses a hexagonal primitive unit cell with space groups of P-6 m2 (No. 187)¹⁶ (figure 1(b)). We relaxed the unit cells and obtained the lattice constant for WSi_2N_4 is $a = b = 2.91$ Å which matches exactly with previously reported results¹⁶. For WGe_2N_4 , the parameters were $a = b = 3.02$ Å. The obtained lattice constants, bond lengths, and bond angles for both structures are shown in Table 1. Here we observed that the bond lengths were increased in the WGe_2N_4 compared to the bond lengths of WSi_2N_4 because the Ge atom has a larger atomic radius than the Si atom.

Table-1: Estimated lattice constants, bond lengths, thickness, and bond angles for monolayer of WSi_2N_4 and WGe_2N_4 .

Structure	a=b (Å)	d(W-N) (Å)	d(X-N) (Å)	Thickness(Å)	$\theta(\text{W-N-W})$	$\theta(\text{N-X-N})$	$\theta(\text{W-N-X})$
WSi_2N_4	2.91	2.10	1.75	10.94	72.96 °	106.62 °	126.47 °
WGe_2N_4	3.02	2.12	1.85	11.54	69.65 °	109.50 °	124.83 °

The cohesive energy gives us information about the stability of the structure of the material. We evaluated the cohesive energy (E_{ch}) for both the structures given by the following formula: $E_{ch} = \{(E_W + 2 \times E_X + 4 \times E_N) - E_{WX_2N_4}\}/7$. Here $E_{WX_2N_4}$, E_W , E_X , and E_N are the energy of the monolayer of WX_2N_4 , the energy of a single W atom, the energy of a single X atom, and the energy of a single N atom, respectively. The cohesive energy per atom obtained for WSi_2N_4 and WGe_2N_4 monolayer was 0.97 eV, and 0.25 eV, respectively, which confirms that these structures are thermodynamically stable. To check the structural stability, we calculated the phonon dispersion curve (shown in figure 2) of WSi_2N_4 and WGe_2N_4 , respectively, along the high symmetry path of Γ -M-K- Γ . No imaginary frequency was found in the phonon dispersion curve, which again confirms the thermodynamical stability of these structures. Since the unit cell of the monolayer contains seven atoms, there are in total twenty-one vibrational modes; the first three are acoustic modes, and the other eighteen the optical modes. The lower three branches correspond to the acoustic vibrational modes, and they are in-plane longitudinal acoustic (LA) mode, transverse acoustic (TA) mode, and out-of-plane mode (ZA). The upper eighteen modes are optical modes. It was observed that for the WGe_2N_4 monolayer, the optical bands overlapped with the acoustic modes, unlike the WSi_2N_4 monolayer, where the acoustic modes are independent.

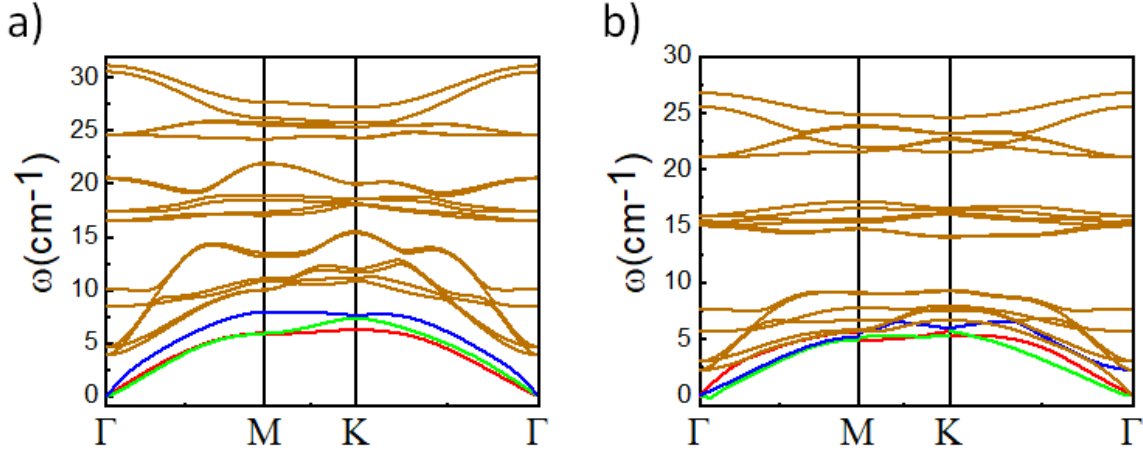


Figure.2: The phonon dispersion plot of the monolayer of a) WSi_2N_4 and b) WGe_2N_4 . The red green and blue colored bands represent ZA, TA, LA bands of acoustic mode.

3.2. Electronic Properties

The electronic band structure of WSi_2N_4 and WGe_2N_4 monolayer was calculated along Γ -M-K- Γ path within an energy range from -4 eV to 4 eV. Figure 3a and 3b show the electronic band structure of WSi_2N_4 and WGe_2N_4 , corresponding BGs of 2.00 eV and 1.15 eV, respectively, according to PBE. The obtained BG value for both materials matched precisely with the previous work by Bohayra Mortazavi et al. ¹⁶. Both the band structures showed an indirect bandgap (BG), and for both the monolayer, the conduction band minima (CBM) are situated at K point. The valance band maxima (VBM) are located at Γ point for WSi_2N_4 , but for WGe_2N_4 , the VBM is situated near the Γ point, which was between the Γ and K points.

The DOS and Local density of states (LDOS) for different orbitals is shown in figure 4 for both monolayers. For WSi_2N_4 , the contribution for VBM is mainly from the p orbitals of N and d orbitals of the W atom, but CBM is contributed primarily by d of the W atom, as shown in the in figure 4(a). For WGe_2N_4 , the primary contribution for VBM is mainly from p of the N atom, and the contribution towards CBM is primarily from the d orbital of the W atom, as shown in figure 4(b). It is observed that for both the monolayer, the N contributes more to the valance band, and W contributes more to the conduction band. p orbital of Si and Ge contributes almost equally toward both the VBM and CBM.

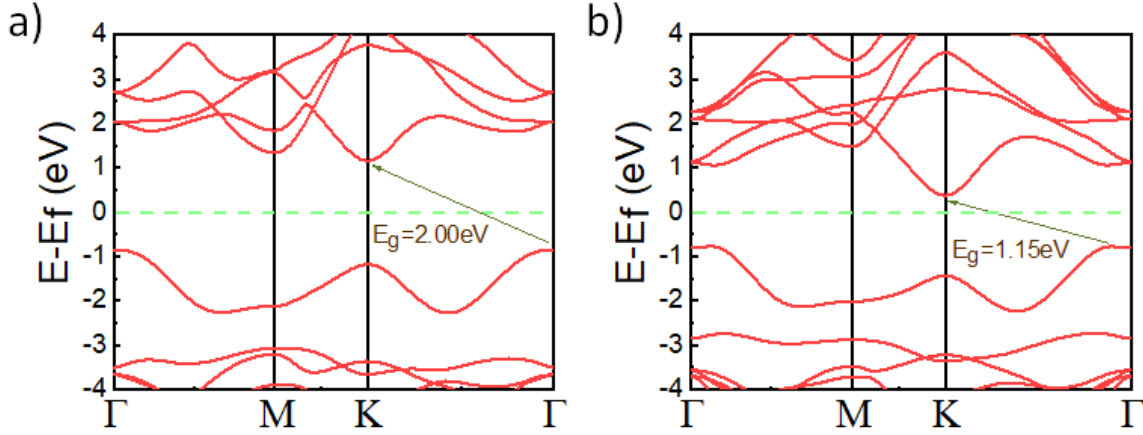


Figure.3: The Band structure of monolayer of a) WSi_2N_4 and b) WGe_2N_4 , with PBE as GGA. The arrow signifies the BG and green dotted lines show the Fermi level.

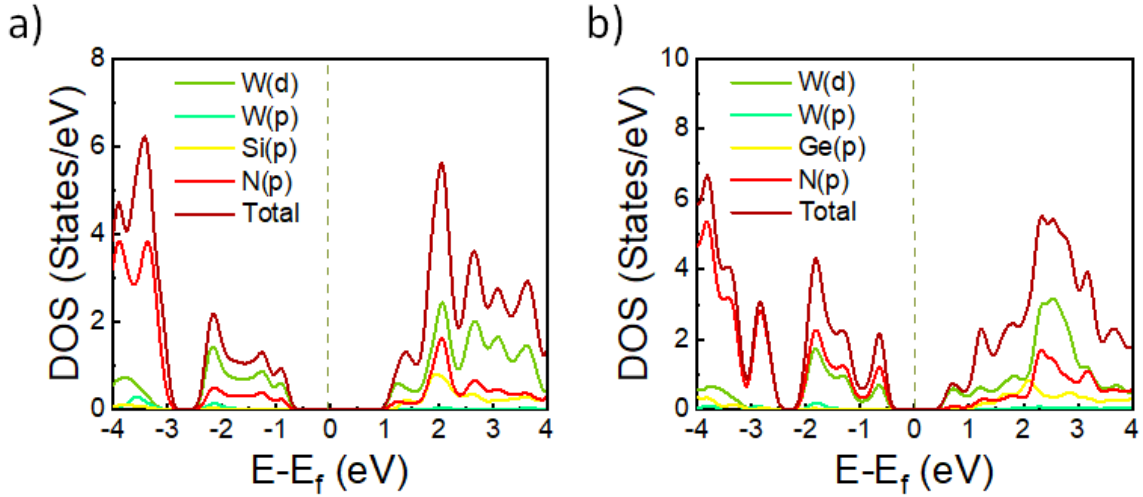


Figure.4: Total DOS with LDOS of the monolayer of a) WSi_2N_4 and b) WGe_2N_4 plotted as a function of energy.

3.3. Carrier mobility and relaxation time

The carrier mobility of electrons and holes for WSi_2N_4 and WGe_2N_4 was predicted by Bohayra Mortazavi et al. They predicted electron mobility (μ_e) and hole mobility (μ_h) was $320 \text{ cm}^2\text{V}^{-1}\text{s}^{-1}$ and $2026 \text{ cm}^2\text{V}^{-1}\text{s}^{-1}$ for WSi_2N_4 and $690 \text{ cm}^2\text{V}^{-1}\text{s}^{-1}$ and $2490 \text{ cm}^2\text{V}^{-1}\text{s}^{-1}$ for WGe_2N_4 monolayer.

Effective mass ($m^* = \frac{d^2E}{dk^2}$) of specific charge carriers can be found from the band edge of band structures. The effective mass of the electron (m_e) can be determined by fitting a parabola at CBM

and operating a double derivative. Similarly, the effective mass of an electron (m_h) can be determined by fitting a parabola at VBM and operating a double derivative. The relaxation time of the charge carrier was calculated by using the well-known formula $\tau = \frac{\mu m^*}{e}$. All calculated parameters for both crystals are listed in table 2.

Crystal	$m_e(Kg)$	$m_h(Kg)$	$\tau_e \times (10^{-14})$ s	$\tau_h \times (10^{-14})$ s
WSi ₂ N ₄	0.254 m_0	0.617 m_0	6.82	71.25
WGe ₂ N ₄	0.243 m_0	0.512 m_0	11.57	72.90

3.4. Optical properties

Optoelectronic device applications require an understanding of optical properties. The optical properties were investigated along the perpendicular direction of the plane. The ϵ_r is obtained using Kramers-Kronig Transformation, and the ϵ_i of dielectric function was calculated using momentum space formulation using proper matrix elements. The dielectric functions were plotted as a function of the energy of photons in figure 5(a) and (b). The ϵ_i shows peak at 3.82 eV for WSi₂N₄, at 3.45 eV for WGe₂N₄. This can be explained by the band structure, as monolayer WGe₂N₄ has 0.85 eV lower BG compared to WSi₂N₄. The secondary peaks were found at 7.27 eV and 6.22 eV, respectively. The peaks were found at 2.55 eV and 1.95 eV for WSi₂N₄ and WGe₂N₄, respectively, for the ϵ_r . The absorption spectra are shown in figure 5(c), and the peaks were found at 4.35 eV and 4.05 eV with absorption coefficient (α) of $2.39 \times 10^5/\text{cm}$ and $2.23 \times 10^5/\text{cm}$ for WSi₂N₄, and WGe₂N₄, respectively, which are of the order of SnI₂, SiI₂,²⁵ ZrS₂ and ZrSSe²⁶. Some secondary peaks are also observed near 8 eV for WSi₂N₄ and near 10 eV for WGe₂N₄ with an even higher absorption coefficient. The variation of refractive index (η) with energy is shown in figure 5(d). At zero energy, the refractive index is found to be 1.78, and 1.90 for WSi₂N₄ and WGe₂N₄, respectively. The secondary peaks are found at energy 2.70 eV and 2.10 eV for and at relatively high energy of 5.85 eV and 5.40 eV for WSi₂N₄ and WGe₂N₄. After 12 eV, the refractive indexes of WSi₂N₄ and WGe₂N₄ are almost the same.

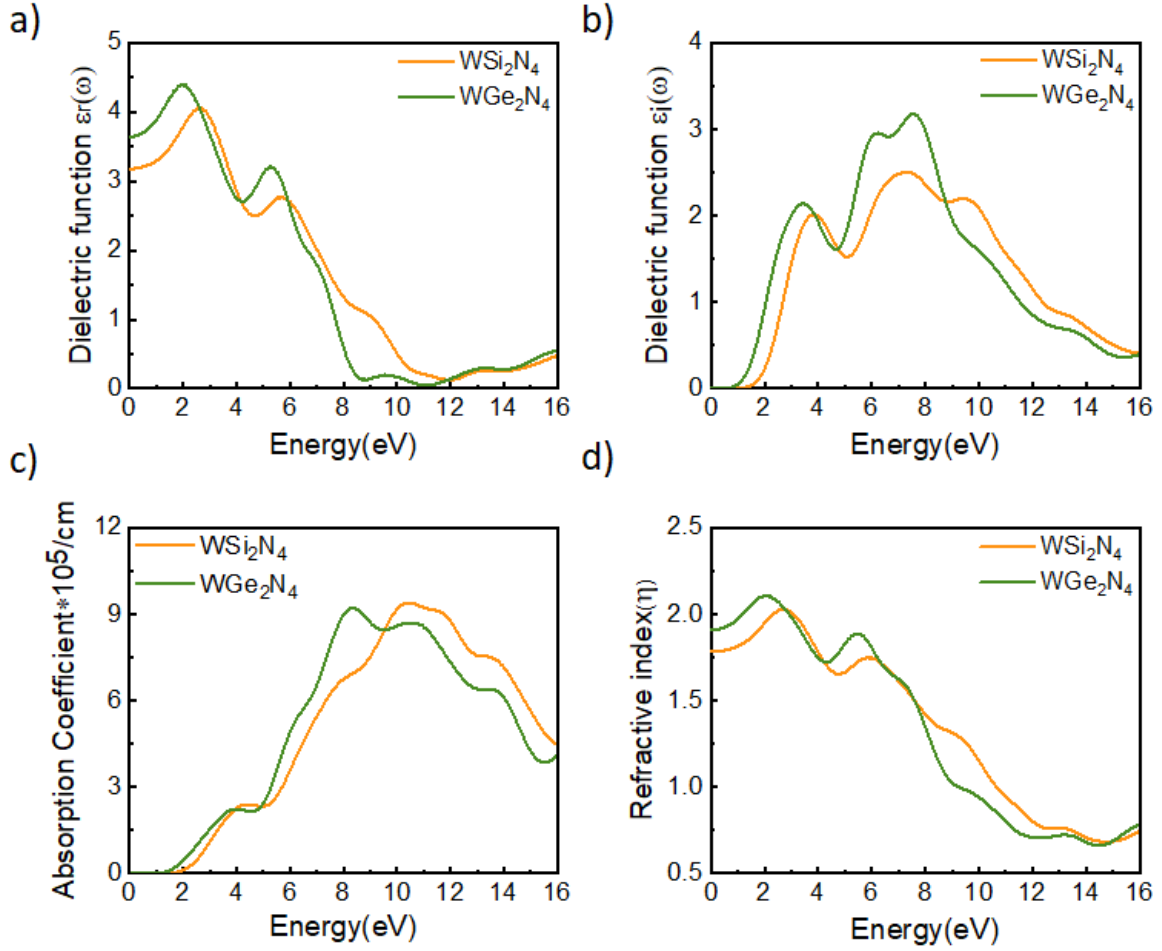


Figure.5: Representation of optical properties a) ϵ_r , b) ϵ_i , c) α , and d) η with respect to energy is shown.

3.5. Thermoelectric Properties

The plot of the Seebeck coefficient (S) with respect to μ at 300 K, 350 K, and 400 K for the monolayer of WSi₂N₄ is shown in figure 6a. The Seebeck coefficient (S) obtained for WSi₂N₄ monolayer at 350 K is 2705.29 μ V/K for n-type carriers ($\mu > 0$) and 2761.84 μ V/K for p-type carriers ($\mu < 0$). At 350 K, the S with increased a little, but after that, it decreased at 400 K. The representation of relaxation time-scaled electrical conductivity (σ/τ) as a function of μ is shown in figure 6b. No such change was found in (σ/τ) for change in T of 100K. The p-type WSi₂N₄ possesses much lower σ/τ compared to the n-type WSi₂N₄. The representation of the relaxation time-scaled power factor ($PF = S^2\sigma/\tau$) as a function of μ is shown in figure 6c for the WSi₂N₄ monolayer. The highest PF was obtained for WSi₂N₄ monolayer for n-type carriers (10.53×10^{10}

W/m²Ks) at 400 K, and for p-type carriers, the highest PF was obtained (4.67×10^{10} W/m²Ks) at 400K. For the WGe₂N₄ monolayer, the variation of S , σ/τ and $S^2\sigma/\tau$ with respect to μ is shown in figure 6d, e, and f. Unlike the WSi₂N₄ monolayer, the S gradually decreases with an increase in temperature. The highest power factor we obtained for the WGe₂N₄ monolayer is 8.60×10^{10} W/m²Ks, which is for the p-type carriers at 400 K, and for n-type carriers, the obtained power factor is 7.51×10^{10} W/m²Ks. So, the p-type doping is much more efficient in WGe₂N₄ towards thermoelectric application. The highest values of S , (σ/τ), ($S^2\sigma/\tau$) for both the monolayers are listed in table 3.

Table 3: Calculated maximum a) S , b) σ/τ , and c) $S^2\sigma/\tau$ for monolayer of WSi₂N₄ and WGe₂N₄.

Crystal	Maximum Seebeck Coefficient(S) (μ V/K)		Maximum Conductivity $\times 10^{19}(\sigma/\tau)$ (S/ms)		Maximum Power Factor $\times 10^{10}$ ($S^2\sigma/\tau$) W/m ² Ks		Thermoelectric figure of merit (ZT)	
	p	n	p	n	p	n	p	n
WSi ₂ N ₄	2761.84	2705.29	1.64	4.82	4.67	10.53	0.26	0.05
WGe ₂ N ₄	1961.78	1935.55	4.00	5.82	8.61	7.51	0.91	0.56

As the Seebeck coefficient (S) is directly proportional to BG^{26} , the S for WSi₂N₄ monolayer was found to be higher compared to WGe₂N₄, which follows the BG trend for the two materials, i.e., WSi₂N₄ has the higher BG value compared to WGe₂N₄.

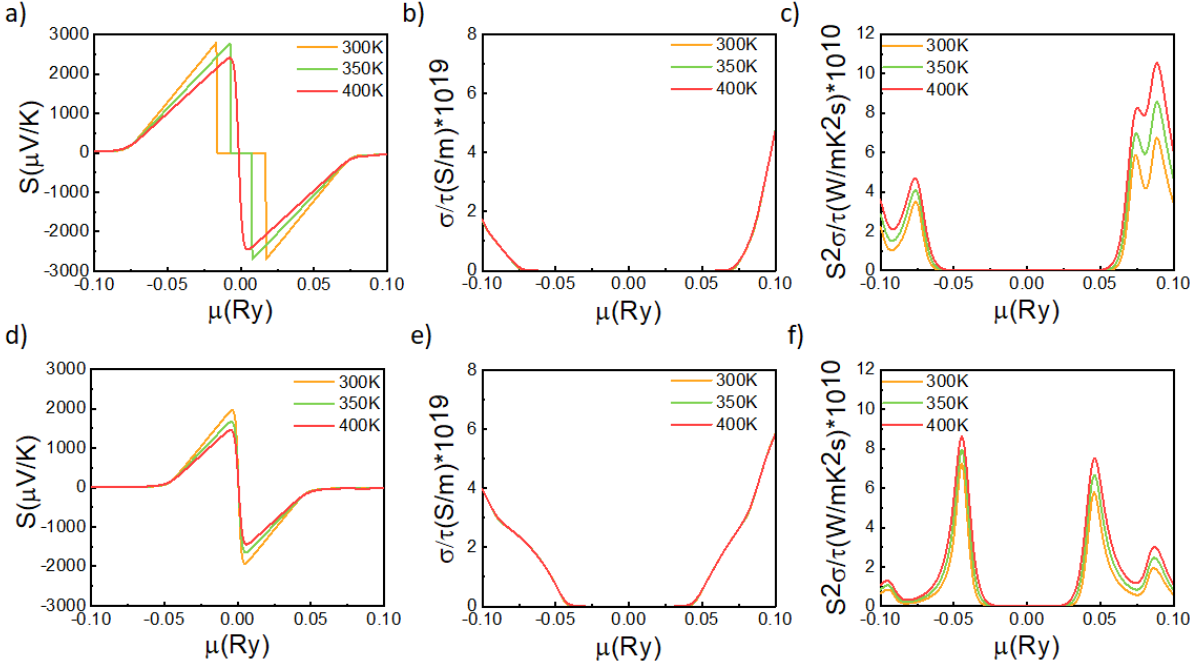


Figure.6: Representation of thermoelectric parameters as a function of μ for WSi_2N_4 monolayer a), b), and c), and for WGe_2N_4 monolayer, d), e), and f).

3.6. Lattice Thermal Conductivity (κ_{ph})

The variation of κ_{ph} with respect to T for monolayer of WSi_2N_4 , and WGe_2N_4 is shown in figure 7a, and 7b. Monolayer of WGe_2N_4 showed significantly lower κ_{ph} (3.63 W/mK) at 300 K, compared to WSi_2N_4 (41.9 W/mK) which are lower than the popular 2D TMDC like MoS_2 (34.5 W/(m.K))²⁷, WS_2 (72 W/(m.K))¹⁷, SnS_2 (15.85 W/(m.K))¹⁴, SiSe_2 (15.85 W/(m.K))²⁸ etc. A decrease in κ_{ph} with an increase in T is observed for both of the structures. The WGe_2N_4 monolayer possesses much lower thermal conductivity compared to monolayer of WSi_2N_4 .

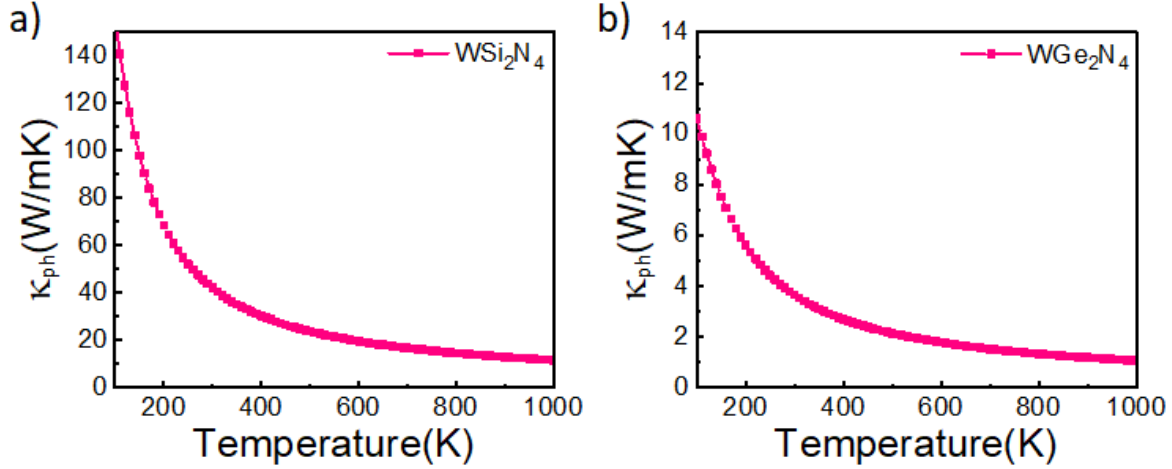


Figure.7: Plot of κ_{ph} with respect to Temperature(K) of monolayer WSi_2N_4 and WGe_2N_4 .

The change of phonon lifetime (τ) and group velocity (G_v) as a function of frequency for both the monolayers is shown in figure 8. The maximum phonon lifetime of WSi_2N_4 (figure 8a) is observed to be much higher than the maximum phonon lifetime of the WGe_2N_4 monolayer (figure 8b). Which is low compared to MoS_2 and WS_2 ^{29,30}. The maximum phonon group velocity obtained for the WSi_2N_4 monolayer is about 11.1 Km/s (figure 8c) which is due to the out-of-plane acoustic mode. Similarly, the maximum obtained G_v for WGe_2N_4 is about 7.5 Km/s (figure 8d) due to the out-of-plane acoustic mode combined with optical modes. As the κ_{ph} is proportional to G_v , and τ , the change in κ_{ph} of the monolayers can be explained easily. As both the τ and G_v for WSi_2N_4 monolayer is much higher than the WGe_2N_4 , the κ_{ph} is much higher in WSi_2N_4 . As from the phonon band structure we can observe that for WSi_2N_4 the acoustic and optical phonon bands are not overlapped, which leads to the increment in κ_{ph} for WSi_2N_4 monolayer. On the other hand, for the WGe_2N_4 , the acoustic and optical phonon bands are overlapped which leads to the decrement of κ_{ph} for WGe_2N_4 monolayer.

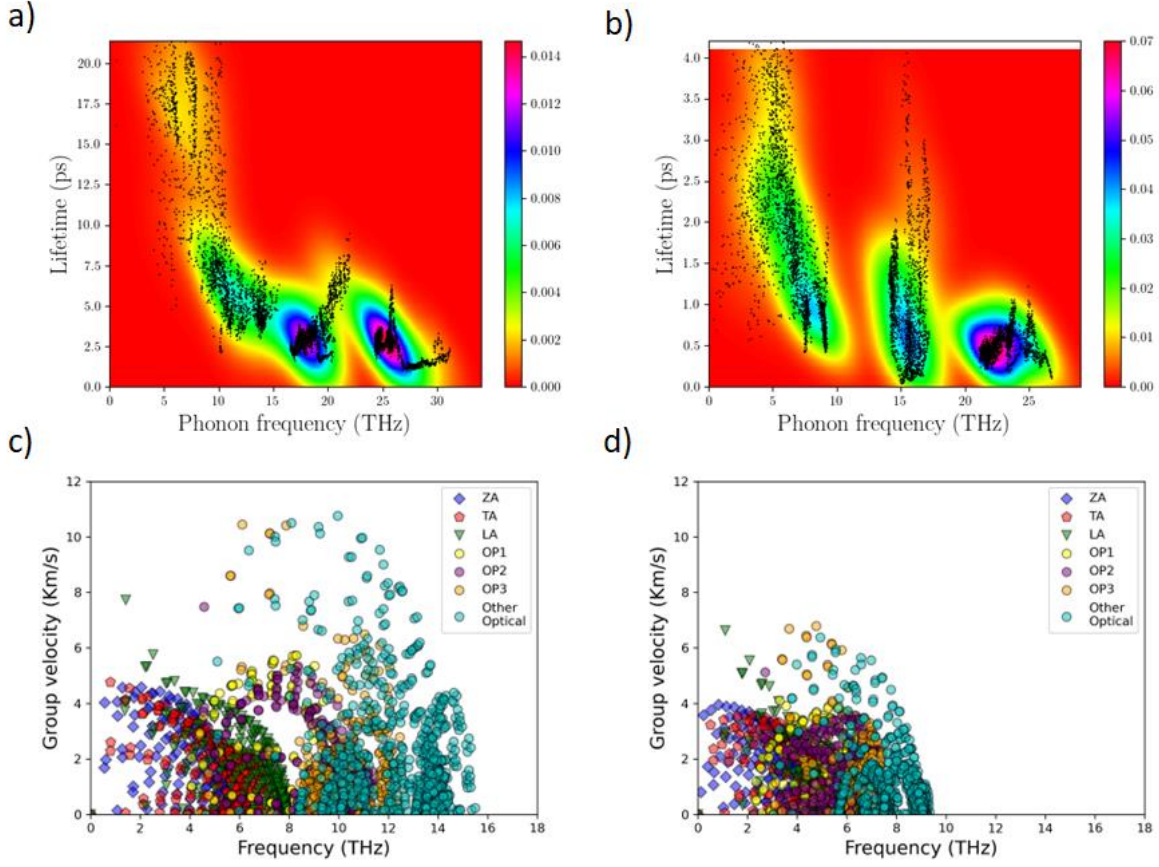


Figure.8: Variation of phonon lifetime with phonon frequency (a) for WSi_2N_4 and (b) WGe_2N_4 monolayer. Variation of group velocity (G_v) for various acoustic and optical modes with the frequency for (c) WSi_2N_4 and (d) WGe_2N_4 monolayer.

3.7. Thermoelectric figure of merit (ZT)

The parameter ZT signifies the efficiency towards the thermoelectric effect along with the quality of a material. To get a high ZT value, we need a high value of σ and a much low value of k ($k_{el} + k_{ph}$) as represented in equation 7. The Thermoelectric figure of merit (ZT) is defined as

$$ZT = \frac{S^2 \sigma T}{\kappa_{el} + \kappa_{ph}} \quad (7)$$

Where S , T , σ , k , and k_{ph} are the same as defined earlier. The obtained ZT product is represented as a function of μ for the monolayer of WSi_2N_4 and WGe_2N_4 at 300 K, 350 K, and 400 K, as shown in figure 9(a) and (b), respectively. Among them, WGe_2N_4 monolayer shows the highest ZT value, i.e., 0.91 for p-type at 400 K and 0.56 for n-type, respectively. On the other hand, the WSi_2N_4 monolayer showed a very low ZT value of 0.26 for p-type and 0.05 for n-type at 400 K. However,

at higher temperatures like 900K, the ZT value reaches around 0.69 (supplementary) for the p-type of WSi_2N_4 monolayer. Both the structures showed higher ZT values towards p-type doping compared to n-type doping. So, for both the structures, the p-type doping (compared to n-type doping) showed a higher ZT value which signifies the effectiveness of p-type doping compared to n-type. The S of WSi_2N_4 is higher rather than WGe_2N_4 , but the σ of WGe_2N_4 is higher than WSi_2N_4 , so the power factor remains comparable, but the k_{ph} played the crucial role in making the WGe_2N_4 monolayer an excellent material towards thermoelectric effect.

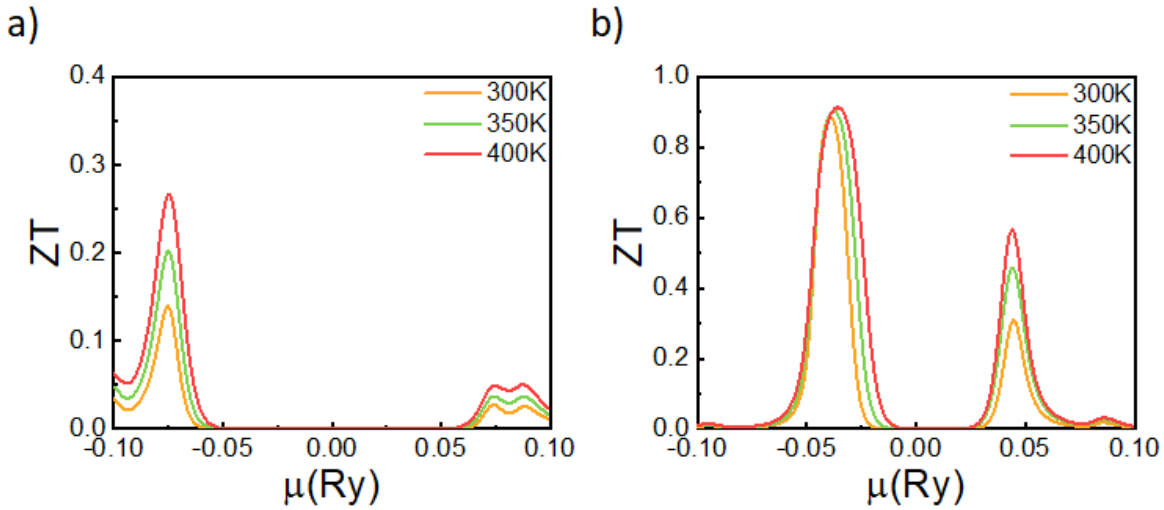


Figure.9: Plot of ZT at different temperatures (T) with respect to chemical potential (μ) for the monolayer of (a) WSi_2N_4 and (b) WGe_2N_4 .

4. Conclusion

We calculated the electronic, optical, and thermoelectric properties using DFT and BTE. The absence of imaginary frequency in phonon dispersion curves proved the dynamical stability of both structures. The ZT and k_{ph} for WGe_2N_4 are found to be outstanding for low-temperature operation. And WSi_2N_4 is not much efficient in the thermoelectric application. An excellent ZT product found is 0.91 for the p-type of WGe_2N_4 at 400 K. So, the WGe_2N_4 monolayer with p-type doping can significantly increase the thermoelectric performance. So, WGe_2N_4 can be used for next-generation low-temperature excellent thermoelectric devices to generate electricity from waste heat.

Acknowledgement:

We are thankful to the Department of Science and Technology (DST), India for supporting us through the INSPIRE program and the Ministry of Human Resource and Development (MHRD). We are also grateful to the Indian Institute of technology Jodhpur for providing the infrastructure to carry out the research.

Reference:

1. Hu, L. *et al.* Tuning multiscale microstructures to enhance thermoelectric performance of n-type Bismuth-Telluride-based solid solutions. *Adv. Energy Mater.* **5**, 1500411 (2015).
2. Zhao, L.-D. *et al.* Ultralow thermal conductivity and high thermoelectric figure of merit in SnSe crystals. *Nature* **508**, 373–377 (2014).
3. Yang, S. H. *et al.* Nanostructures in high-performance (GeTe)_x(AgSbTe₂)_{100-x} thermoelectric materials. *Nanotechnology* **19**, 245707 (2008).
4. Poudel, B. *et al.* High-thermoelectric performance of nanostructured bismuth antimony telluride bulk alloys. *Science* (80-.). **320**, 634–638 (2008).
5. Rhyee, J.-S. *et al.* Peierls distortion as a route to high thermoelectric performance in In₄Se_{3-δ} crystals. *Nature* **459**, 965–968 (2009).
6. Liu, H. *et al.* Copper ion liquid-like thermoelectrics. *Nat. Mater.* **11**, 422–425 (2012).
7. Wang, Y., Rogado, N. S., Cava, R. J. & Ong, N. P. Spin entropy as the likely source of enhanced thermopower in Na_xCo₂O₄. *Nature* **423**, 425–428 (2003).
8. Robert, R., Romer, S., Reller, A. & Weidenkaff, A. Nanostructured complex cobalt oxides as potential materials for solar thermoelectric power generators. *Adv. Eng. Mater.* **7**, 303–308 (2005).
9. Maensiri, S. & Nuansing, W. Thermoelectric oxide NaCo₂O₄ nanofibers fabricated by electrospinning. *Mater. Chem. Phys.* **99**, 104–108 (2006).
10. Venkatasubramanian, R., Siivola, E., Colpitts, T. & O’quinn, B. Thin-film thermoelectric devices with high room-temperature figures of merit. *Nature* **413**, 597–602 (2001).
11. Duong, A. T. *et al.* Achieving ZT= 2.2 with Bi-doped n-type SnSe single crystals. *Nat. Commun.* **7**, 1–6 (2016).
12. Biswas, K. *et al.* High-performance bulk thermoelectrics with all-scale hierarchical architectures. *Nature* **489**, 414–418 (2012).
13. Eda, G. *et al.* Coherent atomic and electronic heterostructures of single-layer MoS₂. *ACS Nano* **6**, 7311–7317 (2012).
14. Karak, S., Bera, J., Paul, S., Sahu, S. & Saha, S. Low thermal conductivity and interface thermal

- conductance in $\text{Sn}\{\text{S}\}_2$. *Phys. Rev. B* **104**, 195304 (2021).
15. Hong, Y.-L. *et al.* Chemical vapor deposition of layered two-dimensional MoSi₂N₄ materials. *Science* (80-.). **369**, 670–674 (2020).
 16. Mortazavi, B. *et al.* Exceptional piezoelectricity, high thermal conductivity and stiffness and promising photocatalysis in two-dimensional MoSi₂N₄ family confirmed by first-principles. *Nano Energy* **82**, 105716 (2021).
 17. Bera, J. & Sahu, S. Strain induced valley degeneracy: a route to the enhancement of thermoelectric properties of monolayer WS₂. *RSC Adv.* **9**, 25216–25224 (2019).
 18. Bera, J., Betal, A. & Sahu, S. Spin orbit coupling induced enhancement of thermoelectric performance of HfX₂ (X= S, Se) and its Janus monolayer. *J. Alloys Compd.* **872**, 159704 (2021).
 19. Kresse, G. & Furthmüller, J. Efficient iterative schemes for ab initio total-energy calculations using a plane-wave basis set. *Phys. Rev. B* **54**, 11169 (1996).
 20. Blöchl, P. E. Projector augmented-wave method. *Phys. Rev. B* **50**, 17953 (1994).
 21. Perdew, J. P., Burke, K. & Ernzerhof, M. Generalized gradient approximation made simple. *Phys. Rev. Lett.* **77**, 3865 (1996).
 22. Soler, J. M. *et al.* The SIESTA method for ab initio order-N materials simulation. *J. Phys. Condens. Matter* **14**, 2745 (2002).
 23. Boukamp, B. A. A linear Kronig-Kramers transform test for immittance data validation. *J. Electrochem. Soc.* **142**, 1885 (1995).
 24. Madsen, G. K. H. & Singh, D. J. BoltzTraP. A code for calculating band-structure dependent quantities. *Comput. Phys. Commun.* **175**, 67–71 (2006).
 25. Betal, A., Bera, J. & Sahu, S. Low-temperature thermoelectric behavior and impressive optoelectronic properties of two-dimensional XI₂ (X= Sn, Si): A first principle study. *Comput. Mater. Sci.* **186**, 109977 (2021).
 26. Das, C. *et al.* Thermoelectric performance and optoelectronic properties of Janus monolayer of ZrXY (X= O, S)(Y= S, Se). *Comput. Mater. Sci.* **218**, 111993 (2023).
 27. Yan, R. *et al.* Thermal conductivity of monolayer molybdenum disulfide obtained from temperature-dependent Raman spectroscopy. *ACS Nano* **8**, 986–993 (2014).
 28. Bera, J., Betal, A., Singh, Z., Gandi, A. N. & Sahu, S. Low lattice thermal conductivity and its role in the remarkable thermoelectric performance of newly predicted SiS₂ and SiSe₂ monolayers. *Comput. Mater. Sci.* **201**, 110931 (2022).
 29. Cai, Y., Lan, J., Zhang, G. & Zhang, Y.-W. Lattice vibrational modes and phonon thermal conductivity of monolayer MoS₂. *Phys. Rev. B* **89**, 35438 (2014).
 30. Gu, X. & Yang, R. Phonon transport in single-layer transition metal dichalcogenides: A first-principles study. *Appl. Phys. Lett.* **105**, 131903 (2014).